

LA-UR-12-24472

Approved for public release; distribution is unlimited.

Title: Calculating alpha Eigenvalues in a Continuous-Energy Infinite Medium with Monte Carlo

Author(s): Betzler, Benjamin R.
Kiedrowski, Brian C.
Brown, Forrest B.
Martin, William R.

Intended for: MCNP Website



Disclaimer:

Los Alamos National Laboratory, an affirmative action/equal opportunity employer, is operated by the Los Alamos National Security, LLC for the National Nuclear Security Administration of the U.S. Department of Energy under contract DE-AC52-06NA25396. By approving this article, the publisher recognizes that the U.S. Government retains nonexclusive, royalty-free license to publish or reproduce the published form of this contribution, or to allow others to do so, for U.S. Government purposes. Los Alamos National Laboratory requests that the publisher identify this article as work performed under the auspices of the U.S. Department of Energy. Los Alamos National Laboratory strongly supports academic freedom and a researcher's right to publish; as an institution, however, the Laboratory does not endorse the viewpoint of a publication or guarantee its technical correctness.

Calculating α Eigenvalues in a Continuous-Energy Infinite Medium with Monte Carlo

Benjamin R. Betzler¹, Brian C. Kiedrowski², Forrest B. Brown², William R. Martin¹

¹Dept. of Nuclear Engineering & Rad. Sciences, Univ. of Michigan, Ann Arbor, MI, bbetzler@umich.edu

²Monte Carlo Codes Group, Los Alamos National Laboratory, Los Alamos, NM, bckiedro@lanl.gov

1 Introduction

The α eigenvalue has implications for time-dependent problems where the system is sub- or supercritical. We present methods and results from calculating the α -eigenvalue spectrum for a continuous-energy infinite medium with a simplified Monte Carlo transport code. We formulate the α -eigenvalue problem, detail the Monte Carlo code physics, and provide verification and results.

2 Theory

Formulating the α -eigenvalue problem relies on the separability of the neutron flux time-dependence from the space- and energy-dependence in the neutron transport or diffusion equations, describing the neutron flux as the sum

$$\psi(\mathbf{r}, E, \hat{\Omega}, t) = \sum_{i=0}^{\infty} A_i \psi_i(\mathbf{r}, E, \hat{\Omega}) \exp(\alpha_i t). \quad (1)$$

The eigenvalues, α_i , and kinetic modes, $\psi_i(\mathbf{r}, E, \hat{\Omega})$, depend on the system configuration, while the coefficients, A_i , are also dependent on source characteristics. Although completeness of the eigenfunctions has not been rigorously proven, this expansion has empirically shown to be accurate. Note this is not the same space-time factorization seen in the point kinetics equations [1], where the neutron flux is assumed to be the product of amplitude and shape functions, the amplitude function providing most of the information on the reactor power change and the shape function describing the time dependence of the power profile. The eigenvalue with the largest real part, α_0 , the fundamental eigenvalue, corresponds to the asymptotic solution of the system as $t \rightarrow \infty$ and follows the trend:

$$\alpha_0 \begin{cases} > 0 & \text{if supercritical,} \\ = 0 & \text{if critical,} \\ < 0 & \text{if subcritical.} \end{cases} \quad (2)$$

For subcritical systems, Rossi- α or pulsed-neutron experiments measure the decay time of the prompt fundamental α mode. These experiments provide a way of measuring the reactivity of subcritical systems. Such experiments have applications for accelerator-driven subcritical (ADS) systems [2] and commercial reactors [3]. With high-energy sources, ADS systems are able to transmute long-lived nuclear isotopes [4]. Previous studies of calculating higher kinetic modes focus on improving experimental results [5] or improving methods for calculating system reactivity from experimental measurements [6].

Neutron Transport

The time-dependent neutron transport and precursor equations [7] are

$$\begin{aligned} \frac{1}{v} \frac{\partial \psi}{\partial t} + \hat{\Omega} \cdot \nabla \psi + \Sigma \psi(\mathbf{r}, E, \hat{\Omega}, t) &= \iint \Sigma_s(E' \rightarrow E, \hat{\Omega} \cdot \hat{\Omega}') \psi' dE' d\Omega' \\ &+ \iint \frac{\chi_p}{4\pi} (1 - \beta) \bar{v} \Sigma_f \psi' dE' d\Omega' + \sum_j \frac{\chi_j}{4\pi} \lambda_j C_j + Q, \end{aligned} \quad (3)$$

$$\frac{\partial C_j}{\partial t} + \lambda_j C_j(\mathbf{r}, t) = \iint \beta_j \bar{v} \Sigma_f \psi' dE' d\Omega'. \quad (4)$$

Separating the exponential time-dependence out of the precursor concentration and neutron flux yields

$$\begin{aligned} \psi(\mathbf{r}, E, \hat{\Omega}, t) &= \psi(\mathbf{r}, E, \hat{\Omega}) \exp(\alpha t), \\ C_j(\mathbf{r}, t) &= C_j(\mathbf{r}) \exp(\alpha t). \end{aligned}$$

Inserting this factorization into Eqs. (3) and (4) and excluding the external source yields

$$\begin{aligned} \frac{\alpha}{v}\psi + \hat{\mathbf{\Omega}} \cdot \nabla\psi + \Sigma\psi(\mathbf{r}, E, \hat{\mathbf{\Omega}}) &= \iint \Sigma_s(E' \rightarrow E, \hat{\mathbf{\Omega}} \cdot \hat{\mathbf{\Omega}}')\psi' dE' d\mathbf{\Omega}' \\ &+ \iint \frac{\chi_p}{4\pi}(1 - \beta)\bar{v}\Sigma_f\psi' dE' d\mathbf{\Omega}' + \sum_j \frac{\chi_j}{4\pi}\lambda_j C_j, \end{aligned} \quad (5)$$

$$\alpha C_j + \lambda_j C_j(\mathbf{r}) = \iint \beta_j \bar{v} \Sigma_f \psi' dE' d\mathbf{\Omega}'. \quad (6)$$

Equation (5) is similar to the steady-state neutron transport equation except for the extra α/v term, known as the time-absorption term. Current Monte Carlo and deterministic methods for determining the fundamental α eigenvalue use an iterative search on a k -eigenvalue problem to find the α for which $k = 1$. This method treats the time-absorption term differently depending on its sign. If $\alpha > 0$, the time-absorption term combines with the cross section, resulting in a larger effective cross section, $\Sigma_{\text{eff}} = \alpha/v + \Sigma$. If $\alpha < 0$, the time-absorption term effectively moves to the right side of Eq. (5) and is treated as a source [8]. This method ignores delayed neutron precursors, excluding the last term of Eq. (5) from the solution.

Designed for supercritical problems, this α - k iterative search works poorly for prompt subcritical systems. As α becomes increasingly negative, the time-absorption term dominates the fission source, causing problems with the transport calculation. However, if the method accounts for delayed neutron precursors, it becomes more stable for far subcritical systems. Combining Eqs. (5) and (6) yields

$$\begin{aligned} \frac{\alpha}{v}\psi + \hat{\mathbf{\Omega}} \cdot \nabla\psi + \Sigma\psi(\mathbf{r}, E, \hat{\mathbf{\Omega}}) &= \iint \Sigma_s(E' \rightarrow E, \hat{\mathbf{\Omega}} \cdot \hat{\mathbf{\Omega}}')\psi' dE' d\mathbf{\Omega}' \\ &+ \iint \frac{\chi_p}{4\pi}(1 - \beta)\bar{v}\Sigma_f\psi' dE' d\mathbf{\Omega}' + \sum_{j=1}^J \frac{\chi_j}{4\pi} \frac{\lambda_j}{\alpha + \lambda_j} \iint \beta_j \bar{v} \Sigma_f \psi' dE' d\mathbf{\Omega}', \end{aligned} \quad (7)$$

introducing J discontinuities at $\alpha = -\lambda_j$. When $\alpha \rightarrow -\lambda_j$, the last term in Eq. (7) either increases considerably if $\alpha > -\lambda_j$ (approaching from $-\lambda_j^+$) or decreases considerably if $\alpha < -\lambda_j$ (approaching from $-\lambda_j^-$). This introduces J more α 's that will balance Eq. (7). These are known as delayed α eigenvalues with delayed kinetic modes. If the system is very subcritical, $\alpha \approx \lambda_j$. This means the precursor decay constant that is smallest in magnitude, λ_j , limits the fundamental α eigenvalue of a subcritical system. The physical analog for this behavior is that when a reactor is shut down, there are still delayed neutron precursors present in the fuel. Those precursors continue to decay and emit delayed neutrons. Thus, the flux does not decay away any faster than the decay of the longest lived precursor group.

Finding an α eigenvalue that is near these discontinuities with the α - k iterative search is numerically difficult. In many problems, the fundamental prompt α eigenvalue, the smallest α eigenvalue not associated with the delayed kinetic modes, is of more interest. Also, the α - k iterative search is computationally costly. Accelerations studied for this method focus on better initial guesses for α [9]. Other methods explored for α -eigenvalue searches include Green's functions [10], diffusion theory approximations [11], and other Monte Carlo methods [12].

Matrix Equation

Instead of using an iterative approach, we directly solve for the α eigenvalue. Introducing operator notation into Eqs. (5) and (6) and rearranging terms yields the forward matrix α -eigenvalue problem

$$\begin{bmatrix} v & 0 \\ 0 & 1 \end{bmatrix} \begin{bmatrix} -\mathbf{L} + \mathbf{F}_p & \chi_d \lambda_j \\ \mathbf{F}_d & -\lambda_j \end{bmatrix} \begin{bmatrix} \psi(\mathbf{r}, E, \hat{\mathbf{\Omega}}) \\ C_j(\mathbf{r}) \end{bmatrix} = \alpha \begin{bmatrix} \psi(\mathbf{r}, E, \hat{\mathbf{\Omega}}) \\ C_j(\mathbf{r}) \end{bmatrix}, \quad (8)$$

where the \mathbf{L} operator combines scattering and leakage. Transposing the second matrix in Eq. (8) yields the adjoint α -eigenvalue problem

$$\begin{bmatrix} v & 0 \\ 0 & 1 \end{bmatrix} \begin{bmatrix} (-\mathbf{L} + \mathbf{F}_p)^\dagger & \mathbf{F}_d^\dagger \\ (\chi_d \lambda_j)^\dagger & -\lambda_j \end{bmatrix} \begin{bmatrix} \psi^\dagger(\mathbf{r}, E, \hat{\mathbf{\Omega}}) \\ C_j^\dagger(\mathbf{r}) \end{bmatrix} = \alpha^\dagger \begin{bmatrix} \psi^\dagger(\mathbf{r}, E, \hat{\mathbf{\Omega}}) \\ C_j^\dagger(\mathbf{r}) \end{bmatrix}, \quad (9)$$

where the eigenvalue sets α and α^\dagger are complex conjugates of each another.

Note that the speed matrix, the far left matrix, is left untransposed. This is because in the adjoint formulation, the α/v term still associates the neutron speeds with the α eigenvalue. We take advantage of this and tally the left side of Eq. (9) to obtain the α -eigenvalue spectrum.

Eigenvalue Spectrum

The solution to Eqs. (8) or (9) have a set of α eigenvalues for $i = 0, \dots, \infty$ [13]. As previously discussed, α_0 is the fundamental eigenvalue, guaranteed to be all real with the trend described in Eq. (2). For $i > 0$, α_i may be complex, but must have a negative non-zero real part, regardless of system super- or subcriticality.

Complex α eigenvalues always come in complex conjugate pairs, and only have a physical meaning when used as a pair. They are not a product of noise, but result from physical phenomena. Mathematically, if there are no complex eigenvalues, the flux contribution of every higher mode only decreases. But in a physical system, neutrons slow down and induce fission, emitting neutrons at higher energies. Thus, the flux at a higher energies experiences a decrease as neutrons slow down and an increase as thermal neutrons fission. This oscillatory motion is only describable with complex α eigenvalues. From Eq. (1), consider the sum of two kinetic modes i and j , where α_i and α_j are conjugate pairs

$$\psi_{i+j}(\mathbf{r}, E, \hat{\Omega}, t) = A_i \psi_i(\mathbf{r}, E, \hat{\Omega}) \exp(\alpha_i t) + A_j \psi_j(\mathbf{r}, E, \hat{\Omega}) \exp(\alpha_j t). \quad (10)$$

The flux solution takes the form

$$\psi_{i+j}(\mathbf{r}, E, \hat{\Omega}, t) = [A_i \psi_i(\mathbf{r}, E, \hat{\Omega}) \exp(\text{Im}(\alpha_i)t) + A_j \psi_j(\mathbf{r}, E, \hat{\Omega}) \exp(\text{Im}(\alpha_j)t)] \exp(\text{Re}(\alpha_i)t).$$

The combination of the two terms in the brackets describe an oscillation dictated by the imaginary part of the eigenvalues. An overall exponential decay dictated by the real part of the eigenvalues damps the oscillation, where $\text{Re}(\alpha_i) = \text{Re}(\alpha_j) < 0$. Both the coefficients, A_i , and kinetic modes, $\psi_i(\mathbf{r}, E, \hat{\Omega})$, may have imaginary parts.

Eigenfunction Expansion

The functional expansion [14] of the neutron flux and precursor concentration in matrix form is

$$\begin{bmatrix} \psi(\mathbf{r}, E, \hat{\Omega}, t) \\ C(\mathbf{r}, t) \end{bmatrix} = \sum_{i=0}^{\infty} A_i(t) \begin{bmatrix} \psi_i(\mathbf{r}, E, \hat{\Omega}) \\ C_{j,i}(\mathbf{r}) \end{bmatrix},$$

where the exponential time dependence in $A_i(t)$ is left undefined. Substituting this expansion into Eqs. (3) and (4) yields the matrix problem

$$\sum_{i=0}^{\infty} \frac{dA_i(t)}{dt} \begin{bmatrix} v^{-1} & 0 \\ 0 & 1 \end{bmatrix} \begin{bmatrix} \psi_i(\mathbf{r}, E, \hat{\Omega}) \\ C_{j,i}(\mathbf{r}) \end{bmatrix} = \sum_{i=0}^{\infty} A_i(t) \begin{bmatrix} -\mathbf{L} + \mathbf{F}_p & \chi_d \lambda_j \\ \mathbf{F}_d & -\lambda_j \end{bmatrix} \begin{bmatrix} \psi_i(\mathbf{r}, E, \hat{\Omega}) \\ C_{j,i}(\mathbf{r}) \end{bmatrix} + Q(\mathbf{r}, E, \hat{\Omega}, t).$$

Multiplying the first term on the right side of the equation by the speed matrix and its inverse yields the forward α -eigenvalue problem defined in Eq. (8). Multiplying by the adjoint function $[\psi_n^\dagger(\mathbf{r}, E, \hat{\Omega}) C_{j,n}^\dagger(\mathbf{r})]$ and integrating over space, energy, and angle takes advantage of the orthogonality condition of the forward and adjoint functions

$$\langle \psi_n^\dagger, v^{-1} \psi_i \rangle_{\mathbf{r}, E, \hat{\Omega}} + \langle C_{j,n}^\dagger, C_{j,i} \rangle_{\mathbf{r}} = \gamma_i \delta_{ni},$$

where $\gamma_i = \langle \psi_i^\dagger, v^{-1} \psi_i \rangle_{\mathbf{r}, E, \hat{\Omega}} + \langle C_{j,i}^\dagger, C_{j,i} \rangle_{\mathbf{r}}$. The result is the first-order differential equation

$$\frac{dA_i(t)}{dt} = \alpha_i A_i(t) + \frac{\langle \psi_i^\dagger, Q \rangle_{\mathbf{r}, E, \hat{\Omega}}}{\gamma_i}. \quad (11)$$

Many problems assume that the external source is shut off at $t = 0$, such as a short pulse, or some given flux distribution at time $t = 0^-$. This assumption describes the source as a delta function in time, $Q_0\delta(t)$. Then, for $t > 0$ there is no external source and Eq. (11) has the solution

$$A_i(t) = A_i(0) \exp(\alpha_i t),$$

revealing the exponential time dependence. Operating on Eq. (11) by $\int_{-\epsilon}^{\epsilon} (\cdot) dt$ yields the coefficients

$$A_i(0) = \frac{\langle \psi_i^\dagger, Q_0 \rangle_{\mathbf{r}, E, \hat{\Omega}}}{\gamma_i}. \quad (12)$$

These coefficients determine the contribution of each kinetic mode, $\psi_i(\mathbf{r}, E, \hat{\Omega})$, to the total flux. This formulation presents a complete solution for the approximation of the time-dependence of the neutron flux. Exact time-dependent Monte Carlo, not requiring the separability approximation, has been an area of research for many years but is still computationally costly [15].

Transition Rate Matrix

Up to this point, we have shown rigorous, unsimplified forms of equations considering space and direction. Here, we adopt the simplifications of a continuous-energy infinite medium, and exclude these spatial considerations from the equations.

The product of the speed and adjoint matrices on the left side of Eq. (9) is

$$\mathbf{Q} = \begin{bmatrix} v(-\mathbf{L} + \mathbf{F}_p)^\dagger & v\mathbf{F}_d^\dagger \\ (\chi_d \lambda_j)^\dagger & -\lambda_j \end{bmatrix}. \quad (13)$$

To examine the structure of the \mathbf{Q} matrix, or transition rate matrix, divide the neutron flux into B energy bins and separate the precursor concentration into J groups. With the energy bin discretization, the top left portion of the \mathbf{Q} matrix in Eq. (13) is

$$v(-\mathbf{L} + \mathbf{F}_p)^\dagger = \begin{bmatrix} -v_1(\Sigma_{r1} - \chi_{p1}\bar{\nu}_{p1}\Sigma_{f1}) & v_1(\Sigma_{s1\rightarrow 2} + \chi_{p2}\bar{\nu}_{p1}\Sigma_{f1}) & v_1(\Sigma_{s1\rightarrow 3} + \chi_{p3}\bar{\nu}_{p1}\Sigma_{f1}) & \cdots \\ v_2(\Sigma_{s2\rightarrow 1} + \chi_{p1}\bar{\nu}_{p2}\Sigma_{f2}) & -v_2(\Sigma_{r2} - \chi_{p2}\bar{\nu}_{p2}\Sigma_{f2}) & v_2(\Sigma_{s2\rightarrow 3} + \chi_{p3}\bar{\nu}_{p2}\Sigma_{f2}) & \cdots \\ v_3(\Sigma_{s3\rightarrow 1} + \chi_{p1}\bar{\nu}_{p3}\Sigma_{f3}) & v_3(\Sigma_{s3\rightarrow 2} + \chi_{p2}\bar{\nu}_{p3}\Sigma_{f3}) & -v_3(\Sigma_{r3} - \chi_{p3}\bar{\nu}_{p3}\Sigma_{f3}) & \cdots \\ \vdots & \vdots & \vdots & \ddots \end{bmatrix},$$

where v_b , Σ_{rb} , Σ_{fb} , $\bar{\nu}_{pb}$, and χ_{pb} are the average speed, removal and fission cross sections, average prompt neutrons emitted per fission, and prompt fission emission probability for energy bin b , respectively; and $\Sigma_{sb\rightarrow b'}$ is the scattering cross section from energy bin $b \rightarrow b'$.

This portion of the \mathbf{Q} matrix has two distinct parts: the diagonal and off-diagonal elements. The diagonal element of row b of the matrix is

$$-v_b\Sigma_{rb} + v_b\chi_{pb}\bar{\nu}_{pb}\Sigma_{fb} = -(\text{removal rate from energy bin } b) + (\text{fission rate from energy bin } b \rightarrow b),$$

which is the negative net removal rate from energy bin b . The off-diagonal element of row b and column $b' \neq b$ of the matrix is

$$v_b\Sigma_{sb\rightarrow b'} + v_b\chi_{pb'}\bar{\nu}_{pb}\Sigma_{fb} = (\text{scatter rate from energy bin } b \rightarrow b') + (\text{fission rate from bin } b \rightarrow b'), \quad (14)$$

which is the net removal rate from energy bin $b \rightarrow b'$.

This is similar to a continuous-time Markov process [16], where \mathbf{Q} is known as the transition rate matrix with the form

$$\mathbf{Q} = \begin{bmatrix} -q_{11} & q_{12} & \cdots \\ q_{21} & -q_{22} & \cdots \\ \vdots & \vdots & \ddots \end{bmatrix},$$

where q_{ij} is the transition rate from state i to state j . For example, $q_{bb'}$ is the transition rate from state i , or energy bin b , to state j , or energy bin b' . A neutron transitions from energy bin $b \rightarrow b'$ by scattering or fission, the rates for which are shown in Eq. (14).

This trend extends to the entire \mathbf{Q} matrix in Eq. (13), where the remaining three portions are

$$v\mathbf{F}_d^\dagger = \begin{bmatrix} v_1\beta_1\bar{\nu}_{d1}\Sigma_{f1} & v_1\beta_2\bar{\nu}_{d1}\Sigma_{f1} & \cdots & v_1\beta_J\bar{\nu}_{d1}\Sigma_{f1} \\ v_2\beta_1\bar{\nu}_{d2}\Sigma_{f2} & v_2\beta_2\bar{\nu}_{d2}\Sigma_{f2} & \cdots & v_2\beta_J\bar{\nu}_{d2}\Sigma_{f2} \\ \vdots & \vdots & \ddots & \vdots \\ v_B\beta_1\bar{\nu}_{dB}\Sigma_{fB} & v_B\beta_2\bar{\nu}_{dB}\Sigma_{fB} & \cdots & v_B\beta_J\bar{\nu}_{dB}\Sigma_{fB} \end{bmatrix}, \quad (15)$$

$$(\chi_d\lambda_j)^\dagger = \begin{bmatrix} \chi_{1\rightarrow 1}\lambda_1 & \chi_{1\rightarrow 2}\lambda_1 & \cdots & \chi_{1\rightarrow B}\lambda_1 \\ \chi_{2\rightarrow 1}\lambda_2 & \chi_{2\rightarrow 2}\lambda_2 & \cdots & \chi_{2\rightarrow B}\lambda_2 \\ \vdots & \vdots & \ddots & \vdots \\ \chi_{J\rightarrow 1}\lambda_J & \chi_{J\rightarrow 2}\lambda_J & \cdots & \chi_{J\rightarrow B}\lambda_J \end{bmatrix}, \quad (16)$$

$$-\lambda_j = \begin{bmatrix} -\lambda_1 & & & \\ & -\lambda_2 & & \\ & & \ddots & \\ & & & -\lambda_J \end{bmatrix}, \quad (17)$$

where $\bar{\nu}_{db}$ is the average delayed neutrons emitted per fission, $\chi_{j\rightarrow b'}$ is the probability of a delayed precursor from group j emitting a neutron into energy bin b' , and β_j and λ_j are the delayed neutron fraction and decay constant for precursor group j . Extending the Markov process analog, $q_{b,B+j}$ is the transition rate from state i , or energy bin b , to state j , or precursor group j . A neutron transitions to a precursor group by delayed fission, the rates for which are shown in Eq. (15). This analog applies to the precursor section at the bottom of the \mathbf{Q} matrix: where $q_{B+j,B+j}$ is the transition rate out of precursor group j , and $q_{B+j,b'}$ is the transition rate from precursor group j to energy bin b' . A precursor from group j decays at a rate of λ_j and transitions to energy bin b' according to the delayed neutron emission spectrum, $\chi_{j\rightarrow b'}$. These rates are shown in Eqs. (16) and (17). Thus, we refer to the the \mathbf{Q} matrix in Eq. (13) as the transition rate matrix.

This treatment shares similarities to the fission matrix method. The fission matrix method uses the kernel $F_{i,j}$, the number of fission neutrons born in region i due to one fission neutron born in region j . This is an unnormalized Markov transition rate matrix for a discrete-time process, known as a Markov chain. The \mathbf{Q} matrix is the continuous-time analog, the unnormalized transition rate matrix for neutrons moving out of a given state and into another.

3 Computational Tools

For this analysis, the continuous-energy infinite-medium Monte Carlo transport code is in MATLAB [17] functions to take advantage of linear algebra and visualization tools. We name the code for its purpose, To Obtain Real-Time Eigenvalues (TORTE).

Code Physics

TORTE has approximately 20 modules, 4 testing scripts, and another 8 post-processing scripts with visualization tools. It calculates the elements of the transition rate matrix during a k -eigenvalue power iteration calculation. It handles multigroup systems with user-specified cross sections or continuous-energy problems using ACE-formatted cross sections. For continuous-energy physics, TORTE considers elastic scattering isotropic and does not model inelastic scattering for fast neutrons. For thermal neutrons, it uses the free-gas model and continuous-S(α,β) scattering tables for graphite. It samples both delayed and prompt fission spectra from the cross section files using ENDF Law 4 [18]. TORTE currently handles the most common reactor materials such as carbon, hydrogen, oxygen, graphite, ^{235}U , and ^{238}U . It treats capture and fission as analog.

Tallying the Transition Rate Matrix

TORTE tallies the transition rate matrix in Eq. (13) using the B energy bins and J precursor groups as discussed. It normalizes the various probabilities such that

$$\begin{aligned}\sum_{b=1}^B \chi_{pb} &= 1, \\ \sum_{b=1}^B \chi_{j \rightarrow b} &= 1, \text{ for } j = 1 \dots, J, \\ \sum_{j=1}^J \beta_j &= 1.\end{aligned}$$

TORTE tallies all matrix elements during the Monte Carlo random walk; it does not use known quantities for decay constants or fractions of delayed precursor groups. All elements are combinations of removal rates and probabilities, such as

$$\begin{aligned}\lambda_j &= \tau_{rj}^{-1} = (\text{average decay time from precursor group } j)^{-1}, \\ v_b \Sigma_{rb} &= \tau_{rb}^{-1} = (\text{average removal time from energy bin } b)^{-1}, \\ v_b \Sigma_{fb} &= v_b \Sigma_{rb} \frac{\Sigma_{fb}}{\Sigma_{rb}} = \tau_{rb}^{-1} \left(\frac{\text{fissions in energy bin } b}{\text{removals from energy bin } b} \right), \\ v_b \Sigma_{sb \rightarrow b'} &= v_b \Sigma_{rb} \frac{\Sigma_{sb \rightarrow b'}}{\Sigma_{rb}} = \tau_{rb}^{-1} \left(\frac{\text{scatters from energy bin } b \rightarrow b'}{\text{removals from energy bin } b} \right).\end{aligned}$$

TORTE uses $J = 6$ precursor groups as is specified in the ENDF cross section database for ^{235}U [19]. The number and size of energy bins is arbitrarily set.

Eigenvalues and Eigenfunctions

TORTE calculates up to $B + J$ α eigenvalues and kinetic modes for the forward and adjoint matrix equations. Because of the infinite medium simplification, the kinetic modes are eigenvectors of length $B + J$, where the first B entries correspond to the neutron flux, and the last J entries correspond to the delayed precursor groups:

$$[\psi(E) \quad C] = [\psi_1 \quad \psi_2 \quad \dots \quad \psi_B \quad C_1 \quad \dots \quad C_{J-1} \quad C_J], \quad (18)$$

where above, ψ_b is the neutron flux in energy bin b and C_j is the concentration of precursor group j . The main interest is in the flux energy spectrum, so the eigenfunction expansion excludes the last J entries of the eigenvector in Eq. (18).

For the simplified continuous-energy infinite medium, the coefficients in Eq. (12) are dot products of the adjoint eigenvectors and desired initial source. The eigenfunction expansion for the neutron flux becomes

$$\psi(E, t) = \sum_{i=0}^N \frac{\psi_i^\dagger(E) \cdot Q_0(E)}{\gamma_i} \psi_i(E) \exp(\alpha_i t),$$

where N is the desired number of modes from $0 \leq N \leq B + J - 1$ used to approximate the flux solution. Generally, as N increases, the flux solution captures increasingly shorter time dependence. If the selection of N includes any complex eigenvalue, it must also include its complex conjugate eigenvalue. The sum of a pair of conjugate eigenvalues from Eq. (10) simplifies to

$$\psi_{i+j}(E, t) = 2[D_1 \cos(|\text{Im}(\alpha_i)|t) - D_2 \sin(|\text{Im}(\alpha_i)|t)] \exp(\text{Re}(\alpha_i)t),$$

where the vectors $D_1 = \text{Re}(A_i) \text{Re}(\psi_i) - \text{Im}(A_i) \text{Im}(\psi_i)$ and $D_2 = \text{Re}(A_i) \text{Im}(\psi_i) + \text{Im}(A_i) \text{Re}(\psi_i)$. This is an underdamped all-real solution with damped frequency $\omega_d = |\text{Im}(\alpha_i)|$. An approximation for the number of oscillations that occur before damping is the ratio $|\omega_d : \text{Re}(\alpha_i)|$.

4 Results

Because TORTE does not include inelastic scattering, results do not match MCNP5 [18] or other transport codes. Thus, we provide comparison to analytic results. We analyze the α -eigenvalue spectrum with some simplified test problems, study the effect of the number of energy bins on the eigenvalue spectrum, make some remarks on eigenvalue convergence, and show results from the eigenfunction expansion.

Physics Verification

To ensure TORTE models collisions and energy distributions properly, we benchmark the results for elastic scattering, free gas scattering, and delayed and prompt fission spectra. Figure 1 compares some spectra against analytic distributions [20]. The results agree, providing confidence in TORTE’s continuous-energy results.

Multigroup Verification

Two multigroup models test TORTE’s ability to calculate the appropriate k eigenvalue and transition rate matrix. The first is a three-group, prompt fission-only model. The second is a three-group model with two precursor groups.

Problem 1: This three-group system has fissions in energy group $g = 3$ emitting $\bar{\nu} = 2.5$ neutrons in energy group $g = 1$. There is no upscatter and downscatter is only allowed into the next group. Table I gives the cross sections and nuclear data of this system.

Table I: Problem 1 nuclear data (cross sections in cm^{-1}).

| g | $\Sigma_{\gamma g}$ | Σ_f | $\Sigma_{sg \rightarrow g+1}$ | χ | $v_g [\text{cm/s}]$ |
|-----|---------------------|------------|-------------------------------|--------|---------------------|
| 1 | 1.0 | 0 | 5.0 | 1.0 | 4.0 |
| 2 | 1.0 | 0 | 4.0 | 0 | 2.0 |
| 3 | 2.0 | 2.0 | 0 | 0 | 1.0 |

The analytic k eigenvalue is

$$k \approx \frac{\bar{\nu} \Sigma_f \Sigma_{s1 \rightarrow 2} \Sigma_{s2 \rightarrow 3}}{\Sigma_{r1} \Sigma_{r2} \Sigma_{r3}} = 0.83333,$$

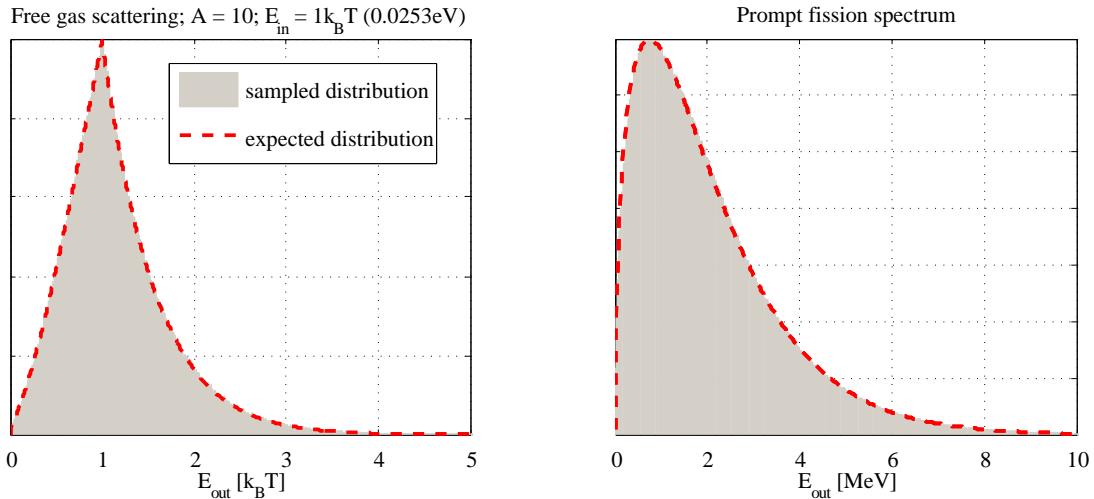


Figure 1: The TORTE free-gas scattering outgoing energy spectrum and $\chi_p(E_{\text{out}})$ agree well with expected analytic distributions: the piecewise free-gas scattering kernel and Watt fission spectrum for thermal neutron-induced fission.

where $\Sigma_{rg} = \Sigma_{\gamma g} + \Sigma_{fg} + \Sigma_{sg \rightarrow g+1}$. The analytic transition rate matrix is

$$\begin{bmatrix} -v_1 \Sigma_{r1} & v_1 \Sigma_{s1 \rightarrow 2} & 0 \\ 0 & -v_2 \Sigma_{r2} & v_2 \Sigma_{s2 \rightarrow 3} \\ v_3 \chi \bar{\nu} \Sigma_f & 0 & -v_3 \Sigma_{r3} \end{bmatrix} = \begin{bmatrix} -24 & 20 & 0 \\ 0 & -10 & 8 \\ 5 & 0 & -4 \end{bmatrix},$$

with $\alpha_0 = -0.44534 \text{ s}^{-1}$. From TORTE with 1×10^6 histories, $k = 0.83377 \pm 0.00059$ and the error in the calculated transition rate matrix is

$$\begin{bmatrix} 0.002 & 0.013 & - \\ - & 0.036 & 0.077 \\ -0.022 & - & 0.025 \end{bmatrix} \%.$$

The analytic k eigenvalue is within one standard deviation of the calculated k eigenvalue and the calculated transition rate matrix is within 0.1% of the analytic transition rate matrix. The calculated α_0 is within one thousandth of a percent of the analytic α_0 .

Problem 2: This three-group system uses two precursor groups to model the emission of $\bar{\nu}_d = 0.5$ delayed neutrons per fission. Other nuclear data is the same as Problem 1. To preserve the k eigenvalue, the Problem 1 $\bar{\nu}$ is taken as the average total neutrons emitted per fission, $\bar{\nu}_t$. All precursors emit neutrons into energy group $g = 1$. Table II gives the delayed neutron precursor data.

Table II: Problem 2 precursor data.

| j | λ_j | β_j |
|-----|-------------|-----------|
| 1 | 3.0 | 0.25 |
| 2 | 1.0 | 0.75 |

The analytic k eigenvalue is the same as in Problem 1 and the analytic transition rate matrix is

$$\begin{bmatrix} -v_1 \Sigma_{r1} & v_1 \Sigma_{s1 \rightarrow 2} & 0 & 0 & 0 \\ 0 & -v_2 \Sigma_{r2} & v_2 \Sigma_{s2 \rightarrow 3} & 0 & 0 \\ v_3 \chi_p \bar{\nu}_p \Sigma_f & 0 & -v_3 \Sigma_{r3} & v_3 \beta_1 \bar{\nu}_d \Sigma_f & v_3 \beta_2 \bar{\nu}_d \Sigma_f \\ \chi_{1 \rightarrow 1} \lambda_1 & 0 & 0 & -\lambda_1 & 0 \\ \chi_{2 \rightarrow 1} \lambda_2 & 0 & 0 & 0 & -\lambda_2 \end{bmatrix} = \begin{bmatrix} -24 & 20 & 0 & 0 & 0 \\ 0 & -10 & 8 & 0 & 0 \\ 4 & 0 & -4 & 0.25 & 0.75 \\ 3 & 0 & 0 & -3 & 0 \\ 1 & 0 & 0 & 0 & -1 \end{bmatrix},$$

where $\bar{\nu}_t = \bar{\nu}_p + \bar{\nu}_d$. The analytic $\alpha_0 = -0.29137 \text{ s}^{-1}$. From TORTE with 1×10^6 histories, $k = 0.83351 \pm 0.00059$ and the error in the calculated transition rate matrix is

$$\begin{bmatrix} -0.158 & -0.121 & - & - & - \\ - & -0.106 & -0.122 & - & - \\ 0.063 & - & -0.073 & -0.052 & 0.101 \\ 0.465 & - & - & 0.465 & - \\ -0.374 & - & - & - & -0.374 \end{bmatrix} \%.$$

Again, the calculated k eigenvalue and transition rate matrix are converging to the analytic solutions. Noticeably, the entries of the transition rate matrix corresponding to delayed neutrons are converging slower than the remainder of the matrix, even with $\bar{\nu}_d$ much higher than in a realistic problem. This is due to the statistical nature of calculating the decay constants, λ_i , and the low probability of delayed fission in comparison to prompt fission. The calculated $\alpha_0 = -0.29414 \text{ s}^{-1}$, and is within 1% of the analytic α_0 .

These two problems verify TORTE's ability to accurately calculate the k eigenvalue and the transition rate matrix for multigroup problems.

Eigenvalue Spectrum

For realistic problems, identifying nuclear processes that affect the calculated α -eigenvalue spectrum is difficult. Thus, TORTE runs variants of a simplified multigroup problem in an effort to explain nuclear effects to the spectrum. Problems 4 and 5 are variations of Problem 3.

Problem 3: This is the base $B = 81$ group system for examining the α -eigenvalue spectrum. Neutrons downscatter only to the next energy group and do not upscatter. Prompt fissions in energy group $g = 81$ emit an average $\bar{\nu} = 2.5$ neutrons per fission into energy group $g = 1$. Table III gives the cross sections and nuclear data of this system. This system has no delayed fissions.

Table III: Problem 3 nuclear data (cross sections in cm^{-1}).

| g | $\Sigma_{\gamma g}$ | Σ_f | $\Sigma_{sg \rightarrow g+1}$ | χ | $v_g [\text{cm/s}]$ |
|------|---------------------|------------|-------------------------------|--------|---------------------|
| 1 | 1.0 | 0 | 100.0 | 1.0 | 1.0 |
| 2-80 | 1.0 | 0 | 100.0 | 0 | 1.0 |
| 81 | 1.0 | 100.0 | 0 | 0 | 1.0 |

The capture cross sections, $\Sigma_{\gamma g}$, neutron speeds, v_g , and removal cross sections, Σ_{rg} , are the same for all groups so that this very unphysical system yields a simple, closed-form solution for the k eigenvalue and α -eigenvalue spectrum. The analytic k eigenvalue is

$$k = \frac{\bar{\nu} \Sigma_f (\Sigma_{sg \rightarrow g+1})^{B-1}}{(\Sigma_{rg})^B} = 1.11663,$$

and is within two standard deviations of the TORTe eigenvalue calculated with 1×10^6 histories, $k = 1.1170 \pm 0.0012$. Algebraic manipulation of the multigroup equations [21] yields the analytic α -eigenvalue spectrum

$$\frac{\alpha_n}{v} = -\Sigma_{\gamma g} + \Sigma_{sg \rightarrow g+1} [\bar{\nu}^{B-1} \exp(2\pi i n B^{-1}) - 1], \quad (19)$$

where $n = 0, \dots, B - 1$. The analytic α eigenvalues form a spectrum in the complex plane along a circle centered at $\text{Re}(\alpha) = -\Sigma_{\gamma g} - \Sigma_{sg \rightarrow g+1}$ of radius $\bar{\nu}^{B-1} \Sigma_{sg \rightarrow g+1}$, where $\alpha_0 = 0.13765 \text{ s}^{-1}$. As B increases, the α -eigenvalue spectrum shrinks because the problem k eigenvalue changes. However, if the group cross sections are adjusted such that the k eigenvalue is the same but the number of groups increases, the α eigenvalues fill in along the existing circle. Figure 2 compares the analytic α eigenvalues against the calculated spectrum. The eigenvalues agree well with the analytic solution, with the eigenvalues with the smallest real parts showing the best agreement.

For this case, there is only one all-real eigenvalue, the fundamental eigenvalue, $\alpha_0 = 0.13839 \text{ s}^{-1}$. The calculated α_0 is within 1% of the analytic α_0 . All higher kinetic modes contribute some oscillatory time dependence to the total flux. Furthermore, there are oscillations that persist for long times, shown by

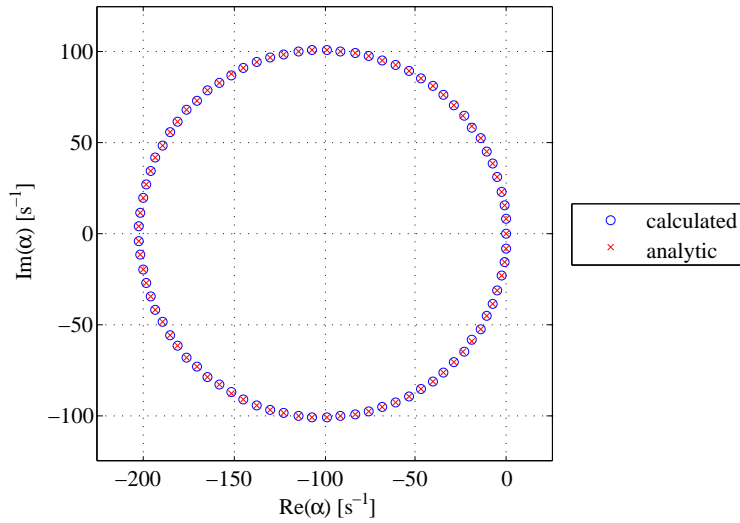


Figure 2: The 81-group Problem 3 α -eigenvalue spectrum forms a circle in the complex plane.

the higher α eigenvalues that have a real part close to that of the fundamental eigenvalue. This is very unphysical. The eigenvalues with the largest imaginary parts are not the largest in amplitude, but are the fastest oscillating.

To better understand this eigenvalue spectrum, we examine the time-dependent flux spectrum from the eigenfunction expansion, given for select times in Figure 3, which compares the approximated solution using all 81 modes to the fundamental mode solution. The source for the eigenfunction expansion is monoenergetic in energy group $g = 1$, where $Q_0(1) = 5 \times 10^4 \text{ cm}^{-3} \cdot \text{s}^{-1}$.

We explain the four subplots of Figure 3 from top left to bottom right: ($t = 0.10 \text{ s}$) Neutrons from the monoenergetic source scatter out of energy group $g = 1$ at different times, resulting in a small flux packet that begins to downscatter. ($t = 0.70 \text{ s}$) The flux packet continues to widen and decrease due to the different rates at which neutrons downscatter and neutron capture. When neutrons reach energy group $g = 81$, they induce fission and emit neutrons in energy group $g = 1$. ($t = 1.60 \text{ s}$) The flux packet widens to the point where it combines with the neutrons fissioning into energy group $g = 1$. ($t = 6.00 \text{ s}$) The flux packets are no longer discernible as the flux distribution approaches and follows the rising fundamental mode.

As $t \rightarrow \infty$, the higher modes decay away and the complete flux solution approaches that of the fundamental mode. For this problem, this happens at $t \approx 20 \text{ s}$, which is long relative to the lifetime of the prompt modes. Delayed modes would persist longer. Note the fundamental mode rises considerably as the higher modes decay. All coefficients, A_i , and eigenvectors, $\psi_i(E)$, are complex for $i = 1, \dots, B - 1$.

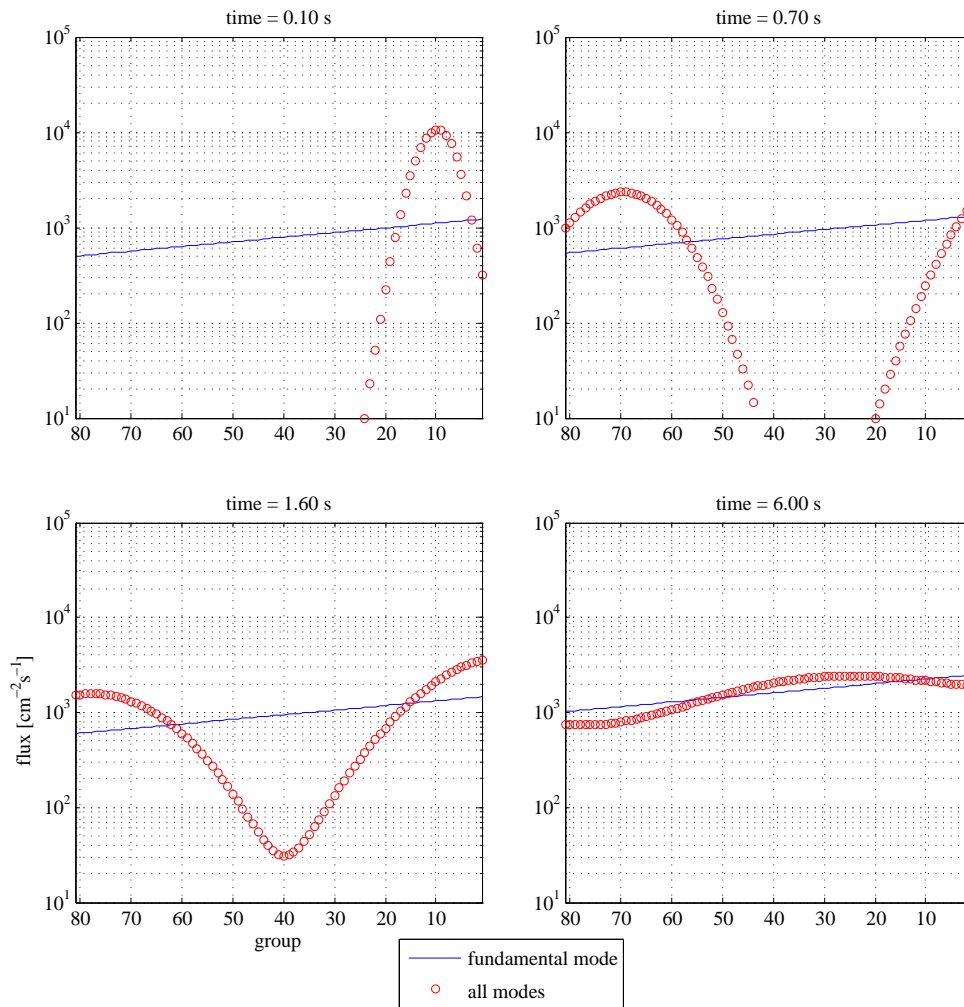


Figure 3: The 81-group Problem 3 approximated flux from the eigenfunction expansion with a monoenergetic initial source for select times.

Problem 4: This variant of the 81-group system changes the speeds to be group dependent, where $v_g = 82 - g$. The k eigenvalue is the same as Problem 3, but the α -eigenvalue spectrum does not have an easily obtainable analytic solution. However, with the analytic transition rate matrix, we obtain the α eigenvalues, and plot them against the calculated results in Figure 4. The analytic $\alpha_0 = 2.2464 \text{ s}^{-1}$. From TORTE with 1×10^6 histories, the analytic k eigenvalue falls within three standard deviations of the calculated, $k = 1.1139 \pm 0.0012$. This is not surprising, as the calculated standard deviation shown is likely smaller than the actual standard deviation due to the system having fissions in only 1 of 81 groups. Thus, we have confidence that TORTE is approaching the proper k eigenvalue. The calculated $\alpha_0 = 2.2008 \text{ s}^{-1}$, and is within 2.5% of the analytic α_0 .

With different group speeds, the eigenvalue spectrum changes significantly. The spectrum has two more very negative real α eigenvalues. The eigenvalues are no longer arranged along a circle, although some elliptical shapes remain. Some eigenvalues form lines crossing the real axis. Again, the eigenvalues closest to the fundamental eigenvalue converge faster than the higher eigenvalues, which are converging slower than in Problem 3.

The extent of the spectrum increases $\sim 25\times$ along the imaginary axis and $\sim 45\times$ along the real axis. This implies an increase of the rate that higher modes are decaying, and an increase in the rate of oscillations. This is due to neutrons moving with a greater speed through the infinite medium space and downscattering faster. The higher modes die quickly, and the complete flux solution approaches the fundamental mode faster than in Problem 3.

Problem 5: This variant of Problem 3 allows downscattering from energy group $g \rightarrow g'$ over several groups with equal probability where $g + 1 \leq g' \leq g + 5$ (except for the last 5 groups, where $g + 1 \leq g' \leq B$). The total downscattering cross section remains the same as Problem 3, but because we are changing the multigroup equations, the k eigenvalue changes considerably, as does the α -eigenvalue spectrum. The analytic $\alpha_0 = 2.2914 \text{ s}^{-1}$. From TORTE with 1×10^6 histories, $k = 1.7676 \pm 0.0464$ and $\alpha_0 = 2.2937 \text{ s}^{-1}$. Figure 4 compares the calculated α -eigenvalue spectrum to the solution from the analytic transition rate matrix.

The spectrum has a cluster of α eigenvalues close to the real axis where $\text{Re}(\alpha) < -100 \text{ s}^{-1}$. These are higher modes that oscillate slowly but decay quickly. There are many more higher eigenvalues in this spectrum than in Problem 3. This is due to neutrons now being able to downscatter quickly by skipping several energy groups, even though the speeds are the same as in Problem 3. As in Problem 4, more higher

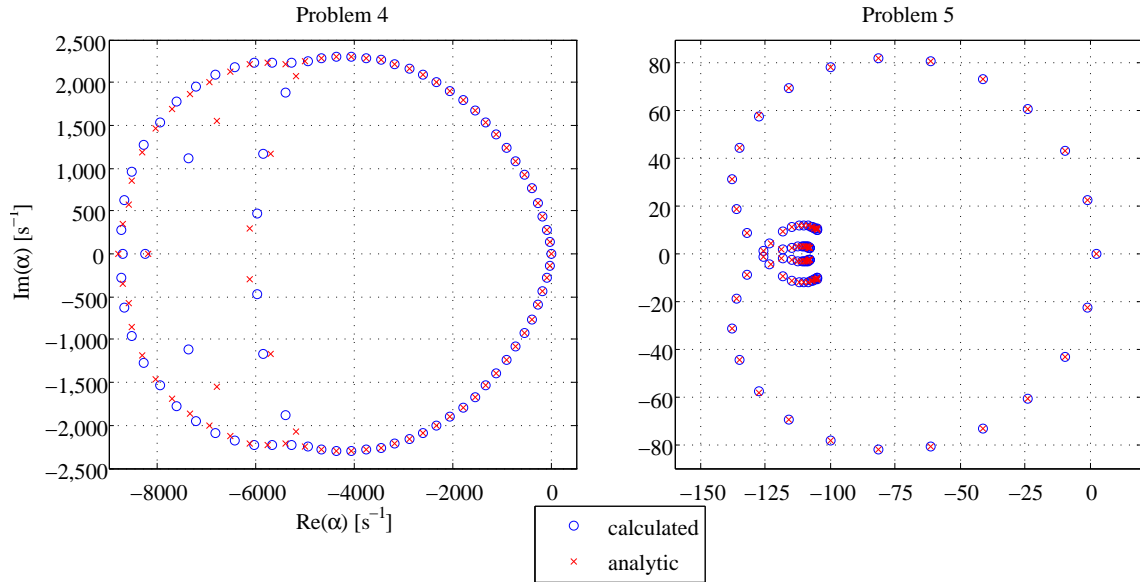


Figure 4: The 81-group Problem 3 variant α -eigenvalue spectra with different group speeds (Problem 4) and downscattering over up to 5 groups (Problem 5) have changed considerably from the base-case circular α -eigenvalue spectrum.

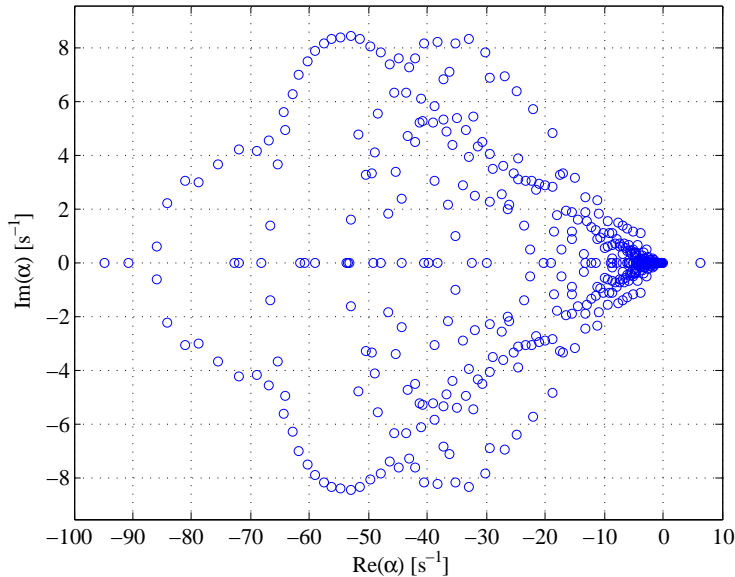


Figure 5: The 641 energy bin Problem 6C α -eigenvalue spectrum for a 1:1:1 H:O: ^{235}U infinite medium shows some similarities to the 81-group problems.

modes decay quickly, but the extent of the spectrum is very similar to that in Problem 3. Thus, there are still oscillatory modes that persist for longer times, and the flux distribution approaches the fundamental mode at a time similar to Problem 3.

Problems 3, 4, and 5 show simplified α -eigenvalue spectra that identify some of the attributes present in the spectrum. Some of these are present in the spectrum from a continuous-energy system in Problem 6, though the spectrum is considerably more complex.

Problem 6C: This continuous-energy system consists of a 1:1:1 atomic ratio of H:O: ^{235}U . The system is very supercritical, with $k > 2.0$. The minimum problem energy is $E_{\min} = 1 \times 10^{-11}$. There are $B - 1 = 640$ equal-lethargy bins between 1.5×10^{-8} and $E_{\max} = 20$ MeV and $J = 6$ delayed neutron precursor groups. Figure 5 shows the α -eigenvalue spectrum from TORTE with $\sim 2.5 \times 10^7$ histories.

There is one large, positive eigenvalue, $\alpha_0 = 6.408 \text{ s}^{-1}$. There is a large cluster of eigenvalues at the right end of the spectrum close to the real axis. The oscillations of these longer-lived modes are relatively slow. There are still elliptical and circular shapes within the spectrum. The scale is considerably different than the 81-group problems due to the realistic neutron speeds, but the relative scale of the real and imaginary axes show more similarities to Problem 4, where each group has a different speed. As in Figure 4, there are several different elliptical shapes and lines of eigenvalues crossing the real axis. Some of the eigenvalues form short irregularly-spaced lines [13].

Energy Bins

To investigate the effect of the number of energy bins on the calculated spectrum, we take Problem 6C and run it with different numbers of equal-lethargy bins.

Problems 6A & 6B: These use the same supercritical, continuous-energy, hydrogenous medium as Problem 6C, but vary the number of energy bins. Table IV describes the energy bin structure and provides brief results of the three Problem 6 runs.

The TORTE energy range is $E_{\min} = 1 \times 10^{-11} \text{ MeV} \leq E \leq E_{\max} = 20 \text{ MeV}$. But, for this far supercritical system, neutrons are unlikely to get to very low energies. Thus, we divide the energy range into $B - 1$ equal-lethargy bins between the two limits E_1 and E_B , the top energy limits of energy bins $b = 1$ and $b = B$, respectively, where the B -th energy bin has E_{\min} as its bottom energy limit.

Figure 6 provides a comparison between the three runs. Most importantly, all three converge to the same positive fundamental α eigenvalue within 0.5%, as shown in Table IV. Some of the higher α eigenvalues

Table IV: Problem 6 energy bin structure and calculated fundamental α eigenvalue (E in MeV).

| Run | B | E_1 | E_B | α_0 [s $^{-1}$] |
|-----|-----|-------|----------------------|-------------------------|
| A | 81 | 20 | 4.1×10^{-8} | 6.396 |
| B | 321 | 20 | 1.5×10^{-8} | 6.413 |
| C | 641 | 20 | 1.5×10^{-8} | 6.408 |

agree, but many do not. In Figure 6, the higher α eigenvalues of Run A fall between those of Run B. There is a similar trend seen in the comparison of Runs B and C, although many more α eigenvalues seem to agree, especially at the front ridges of the spectra. Increasing the number of energy bins does not add higher α eigenvalues to the left end of the spectrum, but adds many α eigenvalues between existing ones.

Theoretically, the system has an infinite set of α eigenvalues, but TORTE uses a finite number of B energy bins and J precursor groups. Thus, by using the transition rate matrix to find the α eigenvalues, TORTE approximates the true infinite α -eigenvalue spectrum with a finite set of eigenvalues. That is the reason the higher eigenvalues of Run A do not match those of Run B. Those higher Run A eigenvalues attempt to capture the true higher α -eigenvalue spectrum, approximating it and falling between the eigenvalues of Run B, which are a better approximation of the true spectrum. But, as the number of energy bins increases, TORTE begins to match the true α -eigenvalue spectrum, and converges to the true eigenvalues in order, from $i = 0, 1, 2, \dots, \infty$. This is seen in comparing Runs B and C, where the α eigenvalues of both runs approach similar α eigenvalues along the front ridges of the spectra.

Conversely, if TORTE uses too few bins, such as 2 or 3, the eigenvalue spectrum converges to an incorrect fundamental eigenvalue, because the transition rate matrix approximates the entire time dependence of the system with too few eigenvalues. This results in an eigenvalue that is often too low. With any of the numbers of energy bins used in Problem 6, TORTE obtains the same fundamental eigenvalue, giving confidence that it has the true fundamental eigenvalue of the system. The first few eigenvalues are most important to the eigenfunction expansion because they are the longest lived. Higher eigenvalues decay very fast, so they are usually much less important.

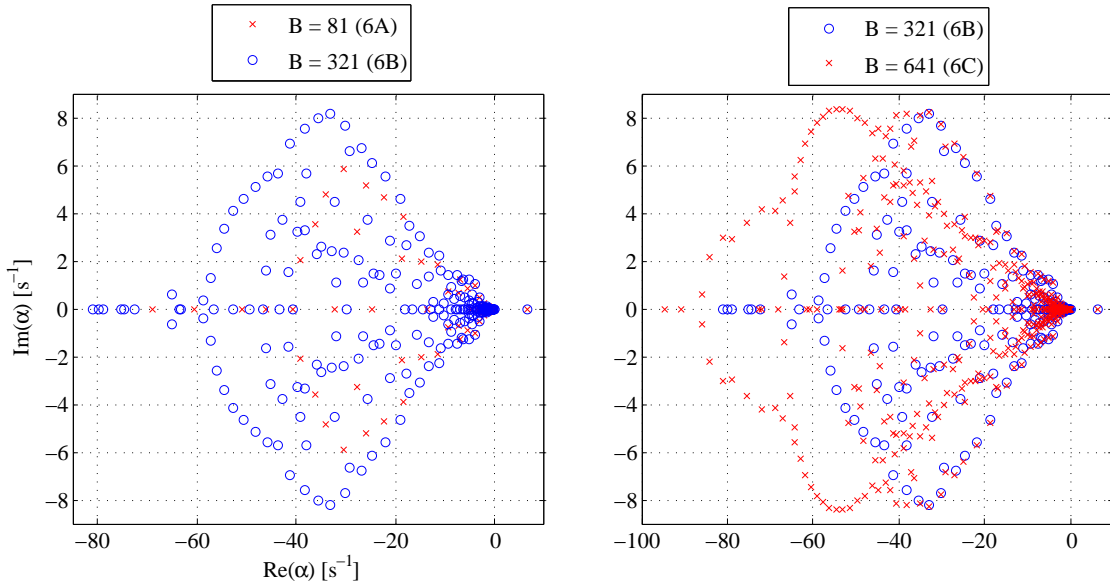


Figure 6: The α -eigenvalue spectra of Problem 6 with different numbers of energy bins show good agreement for the first few eigenvalues but disagree on the shape of the higher α -eigenvalue spectrum.

Eigenvalue Convergence

We use three runs of a delayed-supercritical hydrogenous medium to study the convergence of the eigenvalues and eigenvectors. It is likely that the eigenvalues converge differently depending on the k eigenvalue, and we expect a delayed-supercritical system to converge slower because k is so close to 1. However, other factors such as bin structure and number affect convergence because the calculated spectrum depends on the convergence of the elements, or q_{ij} 's, of the transition rate matrix. As we run more histories, the statistical uncertainty of the tallied removal rates and probabilities, and thus the q_{ij} 's, decreases.

Problems 7A-C: This is a continuous-energy hydrogenous medium with a 6:3:1 H:O:UO₂ molecular ratio. The enrichment is 1.17% ²³⁵U. Three runs explore the effect of the number of equal-lethargy bins on the convergence of eigenvalues. Table V shows the energy bin structure and run characteristics for these variations. All runs use 1×10^5 histories per cycle.

Table V: Problem 7 energy bin structure and total active cycles (E in MeV).

| Run | B | E_1 | E_{B-1} | Cycles |
|-----|-----|-------|----------------------|--------|
| A | 81 | 14 | 5.0×10^{-9} | 100 |
| B | 321 | 15 | 2.5×10^{-9} | 120 |
| C | 641 | 15 | 1.0×10^{-9} | 150 |

For this problem, the TORTE maximum and minimum energies are the same as in Problem 6. But, there are now $B - 2$ equal-lethargy bins between the two limits E_1 and E_{B-1} , the bottom energy limits of energy bins $b = 1$ and $b = B - 1$, respectively. Table VI shows results of the runs.

Table VI: Calculated eigenvalues for Problem 7.

| Run | k eigenvalue | $\alpha_0[s^{-1}]$ | α eigenvalues calculated |
|-----|---------------------|-------------------------|---------------------------------|
| A | 1.0018 ± 0.0004 | 9.4988×10^{-4} | 87 |
| B | 1.0020 ± 0.0004 | 1.3454×10^{-3} | 327 |
| C | 1.0024 ± 0.0003 | 1.4417×10^{-3} | 647 |

All runs converge to the same k eigenvalue within statistical uncertainty. The fundamental α eigenvalue is very near zero and shows much less relative agreement than the calculated k eigenvalue. Figure 7 shows the convergence behavior for the fundamental eigenvalue and eigenvector for each of the three runs. Convergence behavior for Run A ends before Runs B and C because more cumulative histories were run as the energy bins increased. We use the root-mean-square (RMS) of the eigenvector to obtain a single value to measure its convergence, where the RMS is

$$\text{RMS}(\psi) = \sqrt{\frac{1}{B}(\psi_1^2 + \psi_2^2 + \dots + \psi_B^2)}.$$

Figure 7 does not include values calculated before reaching 5×10^5 particles.

Both the fundamental eigenvalue and eigenvector converge. This delayed-supercritical system has a very small α_0 . In terms of percent difference, the calculated α_0 varies considerably over the cycles, but because it is so close to zero, this is not a good measure of convergence. In absolute terms, α_0 varies less than $2 \times 10^{-4} \text{ s}^{-1}$ over the last 25 cycles.

The three runs approach different fundamental α eigenvalues. But, in Problem 6, the calculated α_0 approaches the same value regardless of the number of energy bins. This is only because of the difference in the systems; Problem 6 is far supercritical so its α_0 is on the order of 1 s^{-1} . In Table IV, the α_0 for the three runs varies on the order of $1 \times 10^{-2} \text{ s}^{-1}$, an order of magnitude larger than the Problem 7 α_0 .

In Table VI, the difference between the α_0 of Runs B and C is smaller than the difference between Runs A and B, supporting the assertion that as $B \rightarrow \infty$, α_0 approaches the true fundamental α eigenvalue of the system. Runs B and C converge to nearly the same α_0 , while Run A converges to a very different α_0 , implying that $B = 81$ energy bins is insufficient for calculating the α_0 for this delayed-supercritical system.

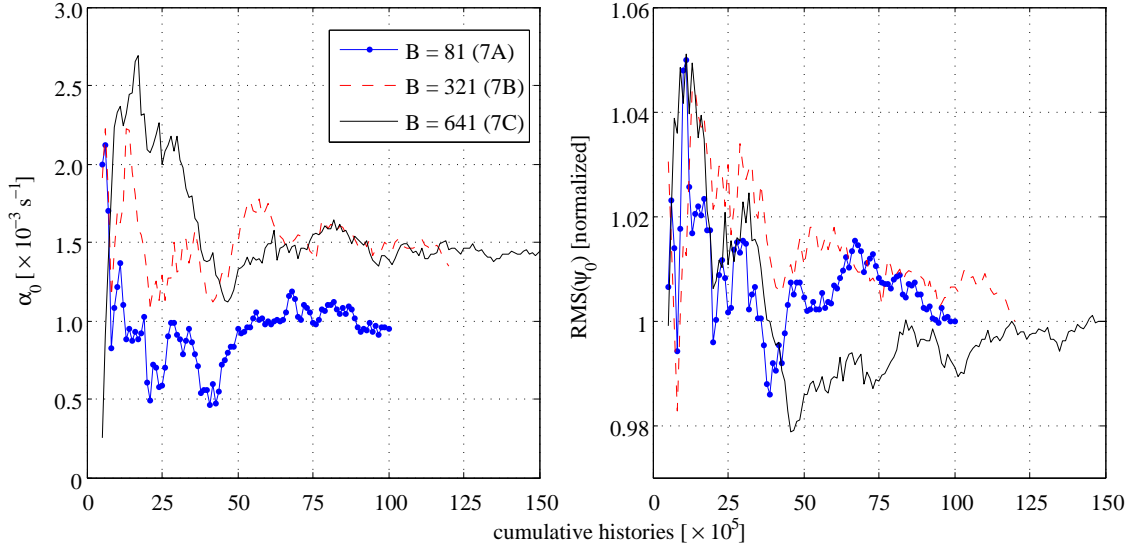


Figure 7: Convergence of the Problem 7A-C fundamental eigenvalues and eigenvectors.

Higher α eigenvalues show similar convergence behavior. However, other than the three α eigenvalues corresponding to the slowest-decaying delayed neutron precursor groups, all higher α eigenvalues are on the order of 10 s^{-1} . These higher α eigenvalues show less relative variation over the cycles, but the absolute variation is greater than that of α_0 . For the three runs, the higher α eigenvalues converge to different values. Thus, the spectrum for each of the runs looks different, as in Figure 6. Higher α eigenvectors show considerable variation over the cycles, and in some cases for the highest α eigenvectors, show little to no apparent convergence and vary up to 100% of the final RMS of the eigenvector. This is in part due to the shape of the highest α eigenvectors being sharply peaked in a few energy bins.

One important factor is how these statistical variations or different spectra affect the eigenfunction expansion. We examine the effect of statistical variation on a given α eigenvalue for two cases: $\alpha > 0$ and $\alpha < 0$.

A positive α eigenvalue only occurs for α_0 when the system is supercritical. Consider a system with the true positive fundamental eigenvalue α_0 and a calculated eigenvalue $\alpha_0 - \epsilon$, where $\epsilon > 0$. Assuming equal coefficients A , the absolute difference between using these two eigenvalues in the eigenfunction expansion is

$$f^+(t) = A \exp(\alpha_0 t) [1 - \exp(-\epsilon t)].$$

As time increases, $f^+(t)$ grows exponentially. For example, take the most different eigenvalues from Problems 6 and 7 in Tables IV and VI. At $t = 10 \text{ s}$, $f^+(t)$ for the problems is 15% and 0.5%, respectively. This is because, even though the Problem 6 α_0 eigenvalues seem to agree better than those from Problem 7, the absolute difference is more important to the eigenfunction expansion. Still, we are more interested in the short-time behavior of the flux spectrum, during which $f^+(t)$ is negligible.

Consider a system with the true negative fundamental eigenvalue α and a calculated eigenvalue $\alpha + \epsilon$, where $\epsilon > 0$. Assuming equal coefficients A , the absolute difference between using these two eigenvalues in the eigenfunction expansion is

$$f^-(t) = A \exp(\alpha t) [\exp(\epsilon t) - 1].$$

In contrast to when α is positive, in the limit as $t \rightarrow \infty$, $f^-(t)$ approaches zero. There is a finite time $t > 0$ where $f^-(t)$ is maximized:

$$t = \frac{1}{\epsilon} \ln \left(\frac{\alpha}{\alpha + \epsilon} \right).$$

Thus, $f^-(t)$ for any negative α eigenvalue is bounded.

Figure 8 compares the flux spectrum using all modes for the three runs. The source strength is set at $Q_0 = 1 \times 10^{15} \text{ cm}^{-3} \cdot \text{s}^{-1}$. The initial source is different for all three runs because the energy bin structures differ. For Run A, a source in energy bin $b = 1$ is actually a square-shaped pulse in energy from E_{max} to E_1 . To match this source for Runs B and C, the initial source is distributed across the appropriate bins. For Run B, the source is spread over the first 5 energy bins and for Run C, the source is spread over the first 9 energy bins. This is still an approximation because the bin structures for the runs do not fall on the same grid, but the difference introduced from this approximation is insignificant.

We explain the four subplots from top left to bottom right: ($t = 0.05 \text{ ms}$) At a very short time after the pulse, the neutrons for all runs downscatter at equal rates and align along the same line. However, the solution from Runs B and C show much more noise than the solution for Run A. This is in part due to the higher eigenvectors not being completely converged for Runs B and C. With fewer eigenvalues, the higher eigenvectors of Run A are more converged. Run A still shows some variation in the lowest energy bins. ($t = 11.0 \text{ ms}$) All runs still agree on the flux spectrum. However, resonances are more resolved with more energy bins in Run C. Run A still shows dips due to resonances, but they are less pronounced. ($t = 1.0 \text{ min}$) All higher kinetic modes are no longer present, and the fundamental mode dictates the shape and time behavior of the solution. Even at this time, the three runs agree considerably well despite the difference in the calculated α_0 . ($t = 1.0 \text{ hr}$) The difference caused by the α_0 's of the runs is not apparent until long times. After an hour, the solution for Run C increases considerably more than Run A. However, if this system is

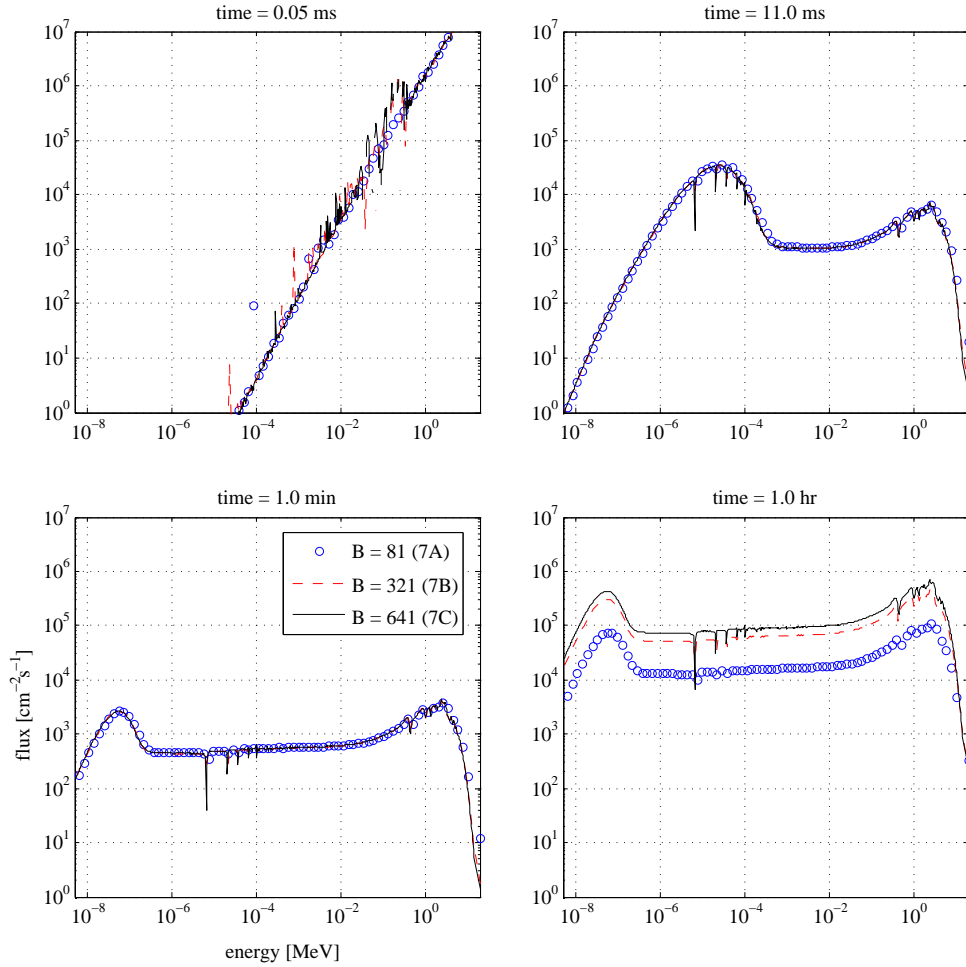


Figure 8: The Problems 7A-C approximated flux spectra from the eigenfunction expansion showing the effect of the different convergence behavior from using different numbers of energy bins.

left unchanged for an hour, temperature and geometry changes will have rendered this solution invalid.

Overall, the flux spectra for all runs agree well despite the difference in the α -eigenvalue spectra and α_0 . This is especially true for the short-time behavior of the flux spectrum.

Flux Transients

To show the usefulness of the eigenfunction expansion to approximate the time-dependent flux spectrum, we select two problems to explore the short time dependence of the solution: a hydrogenous medium and a graphite medium. Both are slightly supercritical systems with $B = 1000$ equal-lethargy bins. To calculate the expansion coefficients for both problems, we use a monoenergetic source in energy bin $b = 1$, $Q_0(1) = 1 \times 10^{15} \text{ cm}^{-3} \cdot \text{s}^{-1}$. This is approximately a 20 MeV pulse.

Problem 8: This is a delayed-supercritical, continuous-energy, hydrogenous medium with a 4:2:1 H:O:UO₂ molecular ratio. The calculated $\alpha_0 = 1.4758 \times 10^{-3} \text{ s}^{-1}$. Figure 9 shows the approximated flux spectrum for selected times.

We explain the four subplots from top left to bottom right: ($t = 0.5 \text{ ms}$) Neutrons from the monoenergetic pulse source begin to downscatter. Flux dips form at high energies as neutrons downscatter past resonances. Because neutrons are able to downscatter to near-zero energies in a collision with hydrogen, a long tail of neutrons extends to lower energies. ($t = 1.5 \text{ ms}$) Neutrons continue to downscatter as the flux at high

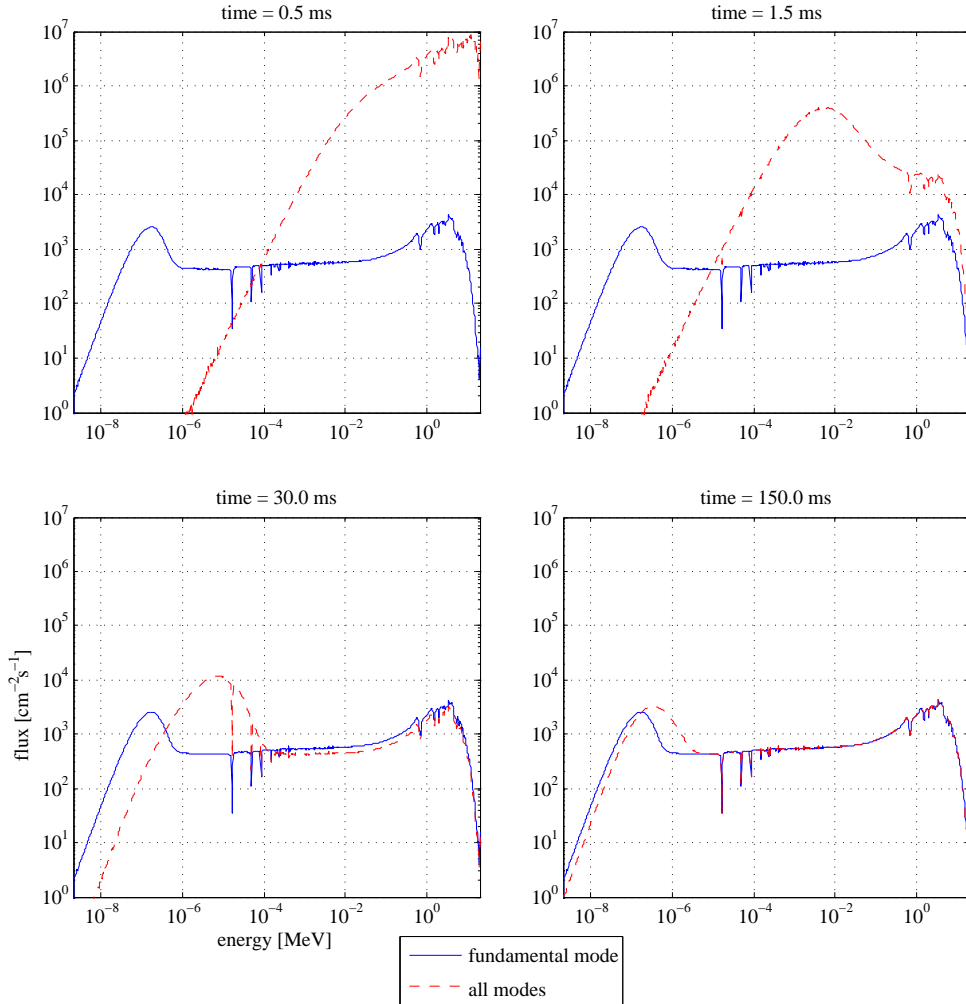


Figure 9: The Problem 8 approximated flux spectrum from the eigenfunction expansion for a monoenergetic high-energy pulse source in a delayed-supercritical hydrogenous medium.

energies finally begins to dip. A very broad flux packet forms. ($t = 30.0$ ms) The flux at high energies continues to decrease and dips below the fundamental mode because the neutrons downscatter out of higher energies faster than they induce fissions and emit neutrons at higher energies. Lower energy resonances cause dips in the flux packet as neutrons downscatter. ($t = 150.0$ ms) The flux at higher energies recovers as neutrons enter thermal energies and induce fission. The majority of the higher kinetic modes decay away and the complete flux solution approaches the fundamental mode solution.

Problem 9: This is a highly-scattering, continuous-energy, graphite medium with a 4000:1 C:UO₂ molecular ratio. It is slightly above delayed supercritical, and the calculated $\alpha_0 = 1.6529 \times 10^{-2} \text{ s}^{-1}$. Figure 10 shows the approximated flux spectrum for selected times.

We explain the four subplots from top left to bottom right: ($t = 0.05$ ms) Neutrons from the monoenergetic pulse begin to downscatter and form a distinct flux packet, as neutrons colliding with carbon cannot scatter to near-zero energies. The flux at higher energies decreases rapidly, as neutrons are not at energies at which fission can replenish the higher energy flux. The peaks below the energy of the flux packet are statistical noise from the eigenfunction expansion attempting to model near-zero flux or very improbable neutrons existing at lower energies. ($t = 0.50$ ms) The distinct flux packet maintains its form and continues to propagate to lower energies. The flux at higher energies decreases considerably and forms dips due to resonances. ($t = 9.00$ ms) The flux packet encounters low energy resonances as the flux at higher energies decreases far below the fundamental mode. Not enough neutrons induce fission because the flux packet is

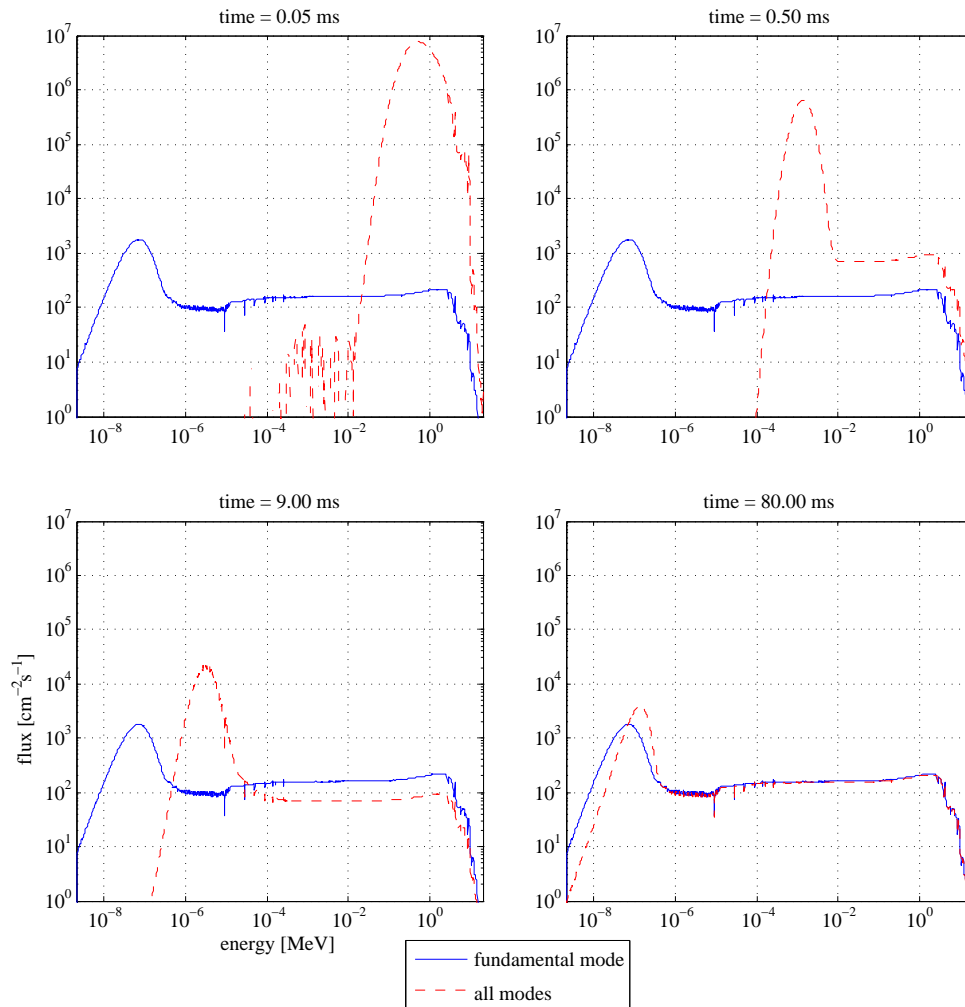


Figure 10: The Problem 9 approximated flux spectrum from the eigenfunction expansion for a monoenergetic high-energy pulse source in a highly-scattering graphite medium.

still above energies at which fission is preferential. ($t = 80.00$ ms) The flux at higher energies recovers due to neutrons inducing fission. The complete flux solution approaches the fundamental mode solution.

With $B = 1000$ energy bins, the neutron flux approximations capture dips in the flux due to cross section resonances. The difference between the two problems in the depth of these resonances is due to the vastly different relative concentrations of moderating nuclei. The flux packet is far more defined in Figure 10 because the neutrons have a minimum non-zero energy to which they can downscatter. This also contributes to the Problem 9 flux at higher energies decreasing below the fundamental mode more than the Problem 8 flux. Furthermore, the flux at higher energies in Problem 9 tends to oscillate more, rising and decreasing several times before approaching the fundamental mode solution. There is a flux hump at higher energies in Problem 8 because of the higher relative concentration of fissile nuclei compared to Problem 9.

In both problems, on the log-log scale in the plots, the fundamental mode solution does not move as the higher modes decay. This far more physical solution is in stark contrast to the Problem 3 flux solution. These are relatively slow transients because $k < 1 + \beta_{\text{eff}}$. We expect the fundamental mode to move faster for a prompt supercritical system. Most of the interesting energy-dependent flux effects occur within a tenth of a second.

Problems 8 and 9 show the potential for use of eigenfunction expansion to approximate the time dependence of the flux spectrum. In both problems, the higher kinetic modes do not decay to the fundamental mode solution for a few seconds. During these first few seconds, the fundamental mode solution is a completely inaccurate representation of the flux spectrum. This flux shape is important for short time transients, pulsed neutron sources, or determining reaction rates for ADS systems. This energy-dependent time behavior is of interest in time-dependent Monte Carlo.

5 Summary

We have a method for calculating the α -eigenvalue spectrum in a continuous-energy infinite-medium. The continuous-time Markov process described by the transition rate matrix provides a way of obtaining the α -eigenvalue spectrum and kinetic modes. These are useful for the approximation of the time dependence of the system.

Performance

The continuous-energy infinite medium Monte Carlo code TORTE accurately calculates the k eigenvalue and transition rate matrix of hydrogenous and graphite media. The calculated eigenvalue spectrum is an approximation to the true infinite α -eigenvalue spectrum. With enough energy bins, TORTE calculates the true fundamental α eigenvalue as well as a few higher eigenvalues. The highest calculated α eigenvalues are an approximation to the actual higher α -eigenvalue spectrum, but still serve to approximate the short-time dependence of the flux.

This method is independent of the k eigenvalue of the system, although the convergence may behave differently depending on how close the system is to critical. The eigenfunction expansion approximates the time-dependent flux for the short time that the fundamental mode is a poor approximation.

Future Work

Ongoing and future work for this method include convergence and comparisons to time dependent Monte Carlo. Convergence conclusions are preliminary and based off of the behavior of a few types of systems. Finding some quantification of the statistical uncertainty of the calculated fundamental eigenvalue is also of interest.

Comparing the approximated fluxes to true time dependent Monte Carlo is useful in quantifying the usefulness of the eigenfunction expansion method and thus the higher kinetic modes. If the approximated flux matches well, then studying the accuracy of the approximation or identifying its weaknesses gives insight to the method. Lastly, introducing leakage and spatial variables to obtain two or three dimensional kinetic modes is of great use in reactor analysis.

References

- [1] S. Dulla, E.H. Mund, and P. Ravetto, “The Quasi-static Method Revisited,” *Progress in Nuclear Energy*, 50, 908-920 (2008).
- [2] C.M. Persson, *et al.*, “Pulsed Neutron Source Measurements in the Subcritical ADS Experiment YALINA-Booster,” *Annals of Nuclear Energy*, 35, 2357 (2008).
- [3] W. Pfeiffer, J.R. Brown, and A.C. Marshall, “Fort St. Vrain Startup Test A-3: Pulsed-Neutron Experiments,” GA-A13079, General Atomic (1974).
- [4] M. Salvatores, I. Slessarev, and M. Uematsu, “A Global Physics Approach to Transmutation of Radioactive Nuclei,” *Nuclear Science and Engineering*, 116, 1 (1994).
- [5] W. Pfeiffer, “RTMODE and RZMODE - Two-Dimensional Computer Codes for Simulating Pulsed-Neutron Experiments,” Gulf General Atomic, Gulf-GA-B10877 (1971).
- [6] Y. Cao and J.C. Lee, “Spatial Corrections for Pulsed-Neutron Reactivity Measurements,” *Nuclear Science and Engineering*, 165, 270-282 (2010).
- [7] G.I. Bell and S. Glasstone, *Nuclear Reactor Theory*, Van Nostrand Reinhold Company, New York (1970).
- [8] D. Brockway, P. Soran, and P. Whalen, “Monte-Carlo Eigenvalue Calculation,” Los Alamos National Laboratory, (1985).
- [9] T.R. Hill, “Efficient Methods for Time Absorption (α) Eigenvalue Calculations,” Los Alamos National Laboratory, LA-9602-MS (1983).
- [10] D.E. Kornreich and D.K. Parsons, “Time-eigenvalue Calculations in Multi-region Cartesian Geometry Using Green’s Functions,” *Annals of Nuclear Energy*, 32, 964-985 (2005).
- [11] K.P. Singh, S.B. Degweker, R.S. Modak, and K. Singh, “Iterative Method for Obtaining the Prompt and Delayed Alpha-modes of the Diffusion Equation,” *Annals of Nuclear Energy*, 38, 1996-2004 (2011).
- [12] Z. Li, *et al.*, “Monte Carlo Simulations and Experimental Validations of α Eigenvalues,” *PHYSOR* (2010).
- [13] E.W. Larsen and P.F. Zweifel, “On the Spectrum of the Linear Transport Operator,” *Journal of Mathematical Physics*, Vol. 15, No. 11 (1974).
- [14] Y. Cao, “Space-Time Kinetics and Time-Eigenfunctions,” Ph.D. dissertation, University of Michigan (2008).
- [15] B.L. Sjenitzer and J.E. Hoogenboom, “General Purpose Dynamic Monte Carlo with Continuous Energy for Transient Analysis,” *PHYSOR* (2012).
- [16] E. Parzen, *Stochastic Processes*, Holden-Day, California (1962).
- [17] MATLAB version 7.10.0, Natick, MA: The MathWorks Inc., 2010.
- [18] X-5 Monte Carlo Team, “MCNP - A General N-Particle Transport Code, Version 5, Volume I: Overview and Theory,” Los Alamos National Laboratory, LA-UR-03-1987 (2003).
- [19] M.B. Chadwick, M. Herman, P. Obložinský, *et al.*, “ENDF/B-VII.1 Nuclear Data for Science and Technology: Cross Sections, Covariances, Fission Product Yields and Decay Data”, *Nuclear Data Sheets*, **112**, pp. 2887 - 2996, 2011.
- [20] E.W. Larsen, “NERS 543: Advanced Nuclear Reactor Theory Lecture Notes,” (2008).
- [21] E.W. Larsen, *Personal Correspondence*, (2012).